IET Renewable Power Generation

Special Issue: Challenges in Future Grid-Interactive Power Converters: Control Strategies, Optimal Operation, and Corrective Actions

IET Journals
The Institution of Engineering and Technology

Energy router for SC: GC, SA and transition mode controls

ISSN 1752-1416
Received on 1st May 2019
Revised 20th October 2019
Accepted on 6th December 2019
E-First on 24th February 2020
doi: 10.1049/iet-rpg.2019.0500
www.ietdl.org

Nuno Vilhena[1], Carlos Roncero-Clemente[2], Vasco Delgado-Gomes[1] ✉, Vitor Fernão Pires[3], João F. Martins[1]

[1]*Faculty of Sciences and Technology, NOVA University of Lisbon, CTS-UNINOVA, 2829-516 Caparica, Portugal*
[2]*Power Electrical and Electronics System Research Group, University of Extremadura, 06006 Badajoz, Spain*
[3]*INESC-ID and Setúbal School of Technology, Polytechnic Institute of Setúbal, 2910-761 Setúbal, Portugal*
✉ *E-mail: vmdg@uninova.pt*

Abstract: From the electrical point of view, the concept of smart community (SC) was defined as a distributed system consisting of a set of smart homes, distributed energy resources (DERs) and energy storage systems (ESSs) using SC controllers to enable smart power management. In this context, the SC energy management system (SCEMS) acts as aggregator of these resources, aiming to assure benefits for every SC stakeholder by setting the SC operation. The references given by the SCEMS must be accurately tracked by the energy routers (ERs), intended as one of the key components of the SC, acting as smart interface between the utility grid and the prosumers' DER and ESS. This study proposes a flexible, robust and simple control strategy for a single-phase ER. The ER regulates the active and reactive powers in grid-connected (GC) mode, and the voltage and frequency when operating in stand-alone (SA) mode. A seamless transition between SA and GC is demonstrated, avoiding undesired transients. The design and implementation of the proposed control strategy is progressively explained. Finally, this is tested via simulation (in PSCAD/EMTDC software) and verified with the experimental prototype.

1 Introduction

Nowadays, there is a shift in the electricity generation and in its management toward the smart grid (SG) approach. The European Technology Platform coined the concept of SG in 2006, defining it as: '*electricity network that can intelligently integrate the actions of all users connected to it-generators, consumers and those that do both to efficiently deliver sustainable, economic and secure electricity supplies*' [1]. At the same time, the attention is also focused on the microgrid/nanogrid, to cope with the high penetration of distributed energy sources (DERs). As a distributed power network, together with the energy storage system (ESS), these architectures are capable of operating in grid-connected (GC) mode and in stand-alone (SA) mode [2–5], depending on the availability of the distributor system operator (DSO).

A more recent concept is the so-called smart communities (SCs), which maximises the DER potential from local resources, providing flexibility and an effective demand-side management [6, 7]. The SC can be defined as a distributed system consisting of a set of smart homes, DER and ESS, which utilise SC controllers (e.g. genetic algorithms and game-theoretic models) to enable smart power management, and to schedule their energy load targeting various purposes, e.g. the electricity bill reduction [8]. In an SC context, the SC energy excess can be consumed by any SC user, and therefore, they become prosumers, defined as an entity that can consume and produce power [9].

The SC includes small-scale ESS, shared by several homes in a community, allowing to store energy for peak shaving and to smooth the unpredictable energy generation from some DER, e.g. photovoltaic (PV) units [10]. The SC control is performed by a central SC energy management system (SCEMS), managing the energy flow between the utility grid, the loads existing in the SC and the different DERs, according to a collaborative strategy to assure benefits for the SC stakeholder [11].

Communication between the SCEMS, other equipment and sensors installed in the SC allows an optimal energy management by the SCEMS, collecting and computing some parameters, e.g. ESS state of charge (SoC), weather forecast, energy prices, load profiles, root-mean-square (RMS) SC grid voltages and frequency at different buses, imbalance coefficients and DSO status. On the basis of different optimisation algorithms [12], SCEMS defines the optimal operation points.

Each DER requires power electronic interfaces that provide an active power flow control (both in DC and AC), tracking the set-points given by the SCEMS. Optimal performance of the power electronic converters can be achieved if they operate in a coordinated way, thanks to the advanced metering infrastructure and the information and communication technologies [13]. In this sense, the trend goes toward the energy router (ER) concept [14].

Focusing the attention on the ER router structure and on its potential interconnections, a single-phase back-to-back converter with DC and AC ports is considered for a nearly zero energy building [14]. The second power stage is composed of a traditional single-phase DC–AC converter, proposing a predictive mode control for the SA operation. A multi-port ER structure is able to interconnect a medium- and low-voltage DC bus, a dedicated bus for the ESS and two AC ports (one to connect to the grid and the second supply AC load) [15]. A similar multi-port configuration is used in [16]. In [17], a three-phase voltage-source-converter-based ER to interlink three microgrids with the distribution network is proposed. Interconnection between multiple DC microgrid clusters can be done by the isolated bidirectional DC–DC converter based on the single-phase and H-bridge topology with a high-frequency isolation transformer [18]. The modular based ER allows the multidirectional power exchange and extends the voltage operation range in the case of DC microgrid clusters [19]. A tri-port converter is considered to act as ER for interconnecting microgrids with corresponding energy management strategies in [20]. Nobel power management strategies and unified control for hybrid AC–DC microgrids are addressed in [21, 22] and [23], respectively.

The stability and robustness in inverter-based droop controlled interconnected microgrids depend on the location of the power electronic units [24–26]. A detailed stability study of a PV-based multiple microgrid cluster and its dynamic behaviour in islanding

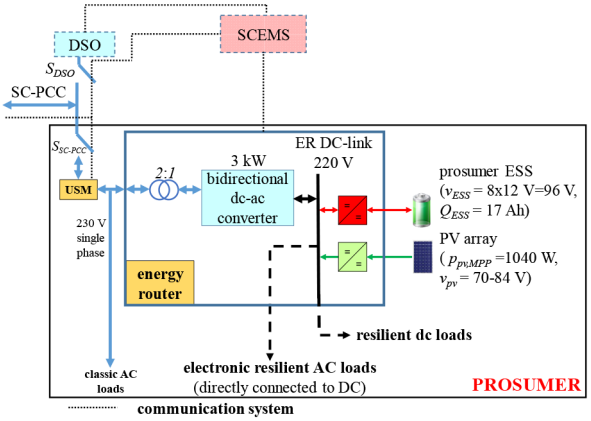

Fig. 1 *ER architecture at the prosumer installation*

mode is reported in [27]. Communication delay compensation strategies in microgrid clusters are reviewed in [28].

The SC electrical energy trading requires that the power converter acting as interface between the DER and AC SC may locally work as current-controlled and voltage-controlled voltage-source inverter [2], providing a seamless connection from SA to GC mode [29]. Furthermore, this seamless transition from SA to GC SC operation allows a reliable utility grid restoration (e.g. in a blackout event), taking the advantage of the distributed ER. If the SC is working in GC mode, the SCEMS sets the active and reactive power references. Otherwise, if the SC is operating in SA, voltage and frequency are set by the SCEMS.

Considering this context and aforementioned challenges, the main contributions of this paper are:

- The proposal of a control strategy for a single-phase ER to control the active and reactive trading between prosumers in an SC.
- A control strategy for the ER to make it capable of operating in SA, controlling the SC voltage and frequency.
- The proposal of a robust control strategy for a seamless and accurate transition from SA to GC. This control allows to exploit the potential of DER to help the power system restoration, e.g. if a blackout occurs, the ER will help performing the black-start operation.
- The experimental validation of the control strategies in an ER prototype.

The developed ER includes one PV system and one ESS; however, both the control strategy and the topology may be extended for more RES or ESS stages.

This paper is organised as follows: first, the ER architecture and its topology are presented and fully described. Second, the proposed control strategy to extract the references derived from the SCEMS set-points in each ER operation mode (GC, SA and transition from SA to GC) are progressively explained. Finally, the ER operation is validated via simulations with PSCAD/EMTDC tool and experiments through an ER prototype.

2 Configuration and structure of the ER

This section describes the main components, the topology and the power stages composing the ER hardware. It is comprised of three power electronic converters, which act as interface between the different energy resources of the prosumers and SC, but other necessary devices, e.g. filters, transformer and control hardware, are also covered.

The main block diagram of the single-phase ER for a prosumer installation is shown in Fig. 1. The ER has as energy resources a PV generation system and an ESS. The DC link of the ER operates at 220 V, to directly supply resilient DC and electronic AC loads. Several power stages and power converters address the different functionalities. A bidirectional single-phase inverter allows the connection with the utility grid, as well as to feed locally the prosumer AC loads.

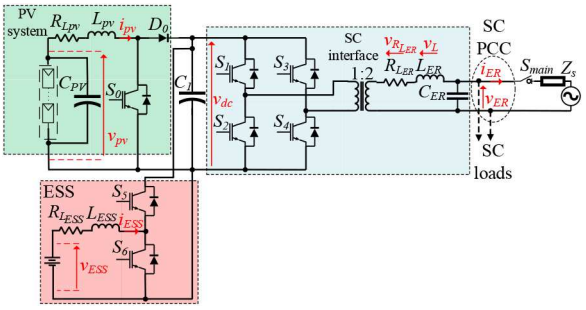

Fig. 2 *Three stages power topology of the implemented ER*

The ER and the unbundled smart metre are located at the prosumer installation sending data to the SCEMS [30]. It also receives information from the DSO and from other sensors (e.g. weather stations, voltage and current sensors installed in smart breakers) available in the SC by a communication system.

A lite SCEMS version was deployed on a Raspberry Pi 3 model B+ with a 64 bit quad core processor running at 1.4 GHz, and dual-band 2.4 and 5 GHz wireless local area network with modular compliance certification. These characteristics allow the SCEMS to run complex algorithms, receiving multiple data from different systems that are connected to the SC and to send optimised ER set-points. The low-level ER controller system is based on the Arduino Due board. This board uses the Atmel SAM3X8E ARM Cortex-M3 CPU (32 bit ARM core microcontroller), able to operate at a maximum frequency of 84 MHz. At the same time, the board includes the required analogue inputs and pulse-width modulation output channels to control the developed ER.

The power stage topology of the single-phase ER is shown in Fig. 2. It includes three power converters sharing a common DC link (capacitor C_1). It is important to note that a larger C_1 capacitor was selected to smooth the low-frequency ripple at the ER DC-bus voltage and of the input currents [31]. The purpose of the used topology is to act as active device between the prosumer and its SC. A conventional DC–DC boost converter, composed of an inductor filter (L_{pv}), a single switch (S_0) and a diode (D_0), connects the PV panels to the ER DC bus (this system is highlighted in green in Fig. 2). A capacitor (C_{PV}) is installed in parallel with the PV array to stabilise the PV array voltage. The main functionality of this converter is the maximum power extraction from the PV array [maximum power point tracking (MPPT)] or to provide any feasible power reference value [reference power point tracking (RPPT)]. The PV system ability to work with the MPPT or RPPT algorithms increase the flexibility of the PV energy production [32].

The ER ESS connection is achieved through a half-bridge bidirectional buck–boost DC–DC converter, composed of two switches (S_5 and S_6), and one inductance (L_{ESS}) (highlighted in red in Fig. 2). In the GC mode, this power converter will demand/inject power from/into the SC, acting as an energy buffer to meet the ER power balance. Besides, it regulates the DC-bus voltage to its reference value when the ER operates in SA mode.

Finally, a full-bridge two-level DC–AC converter is in response of the electrical energy interaction between the prosumer and SC in terms of power trading both in GC and in SA operation. Moreover, this topology allows providing ancillary services. Composed of four switches (S_1–S_4) and an inductor–capacitor filter (L_{ER} and C_{ER}), this DC–AC converter (highlighted in blue colour in Fig. 2) is responsible for the main functionalities and SC services, synchronisation with the SC electric grid and AC classical load supply. This converter topology can afford to include another RES, another kind of ESS and other energy devices to fulfil the SC goals and to meet the set-points given by the SCEMS.

A 1:2 low-frequency transformer is considered before connecting the ER to the SC electric PCC, to provide galvanic isolation and, at the same time, to avoid DC current injection into the SC electric grid. The use of this transformer allows the ER to operate with reduced DC-link voltages, leading to a higher protection level against indirect contacts. Fig. 2 also contains all

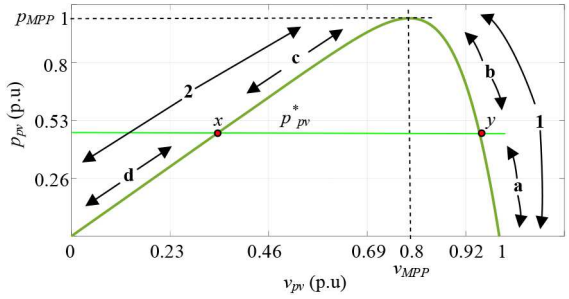

Fig. 3 *Typical P–V curve with the different zones (1 and 2) and subzones (a–d) for the implemented RPPT algorithm*

the electrical variables used in subsequent sections. More details of the ER design, sizing and assembling are described in the following sections.

3 Operation modes and flexible ER control

The proposed ER control strategy is detailed in this section presenting the implementation schemes. The control strategy for the PV system and ESS is first presented, composing the prosumers' energy resources. Then, the ER control strategy for GC, SA and transition modes are progressively explained, presenting the mathematical expressions.

The SCEMS carries out a multi-criteria optimisation algorithm [12], and sends the operation modes, the active power and the reactive reference set-points (p^* and q^*) to each ER (if the ER is operating in GC mode) and also to the different ER power resources (reference power points for the PV converters (p^*_{pv}) and charging/discharging reference points for the ESS (p^*_{ESS}). If the ER is working in SA, the SCEMS sets the references of the RMS grid voltage (V^*_s) and the SC frequency (ω^*). This flexible ER control assumes that the situation where the SC becomes isolated suddenly from the utility grid is not desired (caused by an unexpected grid event) and the anti-island protection algorithm acts to disconnect the ER.

The different control targets that compose the proposed flexible ER control, related to the operation modes and derived set-points from the SCEMS are:

- *Adjustable grid-injected power flow in GC mode:* The active (p) and reactive (q) powers set-points must be accomplished at the SC-PCC. At the same time, the power distribution between the PV and ESS must fulfil the SCEMS optimisation outputs.
- *Accurate voltage/frequency control in SA mode:* If the DSO grid is not available or the SCEMS establishes this operation mode to achieve the SC goals, the ER is feeding AC loads directly, assuring that the RMS SC grid voltage and frequency are within the specifications with the required quality.
- *Seamless transition from SA to GC*: A smooth and safe transition from SA to GC mode must be assured without undesired transients during the main switch turning-on process. A pre-synchronisation is mandatory to provide a zero-inrush current, taking into account the latency of the communication between the SCEMS and ER.

To make easier the understanding of the proposed flexible ER control strategy for the generation of the references and the tracking techniques associated, the following sign criterion is adopted. If the ER is injecting active power to the SC, the set-point is positive ($p^* > 0$) and negative ($p^* < 0$) if the ER is demanding power from the SC. Similar sign criteria is adopted for the reactive power. At the same time, the ESS discharges or charges depending on whether p^*_{ESS} is positive or negative, respectively. Following sections explain the operation strategy implemented for each power conversion stage.

3.1 PV interface

To enhance the ER flexibility, an RPPT algorithm was implemented based on [32]. This algorithm considers a situation, in which p^*_{pv} could be lower than the maximum available in the PV system. RPPT operation is used instead of MPPT due to the saturation limits of the ESS (surpassing its maximum voltage limit could be dangerous), and also the prevention of overvoltage or frequency deviations in some critical periods in certain buses during the SC electric grid operation (also known as active power curtailment technique [33]).

It is important to note that the implemented RPPT algorithm can also operate at the MPP. Several MPPT algorithms have been proposed in the literature, differing in the complexity of implementation, required sensors, converge speed, cost, range of effectiveness and hardware implementation [34]. Three most traditional MPPT algorithms are highlighted due to their capabilities: the perturb and observe (P&O) method, incremental conductance and the method based on dP/dV or dP/dI feedback. The algorithm used in this work is based on the P&O method, improved with adaptive step to maximise the performance and minimise the power fluctuations. A typical P–V curve is shown in Fig. 3, where two different subzones (a and b) placed at the right of the MPP (called zone 1) and another two subzones (c and d) placed at the left of the MPP (called zone 2) are shown. Zones 1 and 2 are distinguished for the MPP tracking; otherwise, zones a, b, c and d must be analysed. There are two feasible PV points in the curve that match a set-point given by the SCEMS (marked as x and y). The one located at the right-hand side of the MPP (within zone 1) is a better choice since the PV voltage will be higher, leading to a reduced D_{pv}. As the DC-link voltage is regulated by the ESS DC–DC converter, the more the D_{pv} rises, the further the system moves to the left-hand side of the P–V curve.

The variables measured to perform the RPPT algorithm are the PV current (i_{pv}) and the PV voltage (v_{pv}) (see Fig. 2). Depending on the observed magnitudes: PV power (p_{pv}) and v_{pv} and their previous values, it is possible to determine the D_{pv} to be applied, that is, to determine the new direction of the perturbation step (δ_{pv}). The direction of δ_{pv} depends on the subzone (a, b, c or d), where the system is operating. In general, three possibilities exist:

i. $p^*_{pv} < p_{MPP}$ and $v_{pv} \geq v_{MPP}$: Desired operation subzones (a and b). The observation of the current measurements together with the previous perturbation direction and measurements will guide the system to the set-point.
ii. $p^*_{pv} < p_{MPP}$ and $v_{pv} < v_{MPP}$: Subzones (c and d) to be avoided. A negative value of δ_{pv} (system displacement to the right-hand side of the P–V curve is mandatory).
iii. $p^*_{pv} \geq p_{MPP}$: The system will reach the MPP.

The truth table to be implemented in the low-level controller to select the following duty cycle (D_{pv}) according to the aforementioned RPPT algorithm is shown in [32]. Once the algorithm achieves a convergence solution and the PV system is working around the RPP or MPP, δ_{pv} is reduced to improve the steady-state performance. The adjustment of δ_{pv} is done by observing the sign of the last perturbations. This iterative process is executed until δ_{pv} gets a minimum value. Similarly, if the direction of δ_{pv} presents the same sign during some perturbations, the value of δ_{pv} is reset progressively until the initial value. This reset is considered to obtain a faster dynamic response during a change in the set-points or in partial shadows condition.

3.2 ESS interface

Some of the optimised solutions of the ESS are based on hybrid solutions. A collaborative strategy consisting of the collaborative association between batteries and supercapacitors are studied in [35, 36]. The control strategy is based on the use of a low-pass filter, which provides a high-frequency reference for the supercapacitor and a low-frequency reference for the battery, with

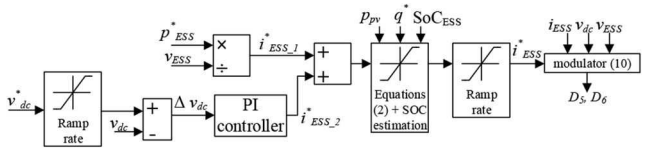

Fig. 4 *Block diagram of the ESS control strategy*

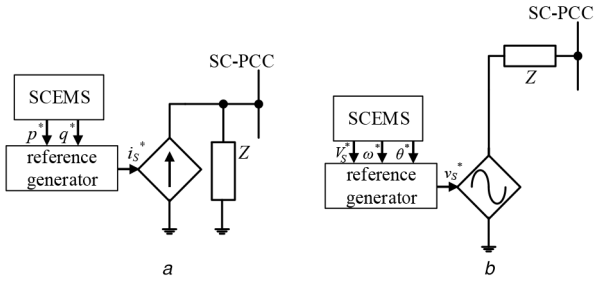

Fig. 5 *ER representation*
(a) ER in GC mode, ***(b)*** ER in SA mode

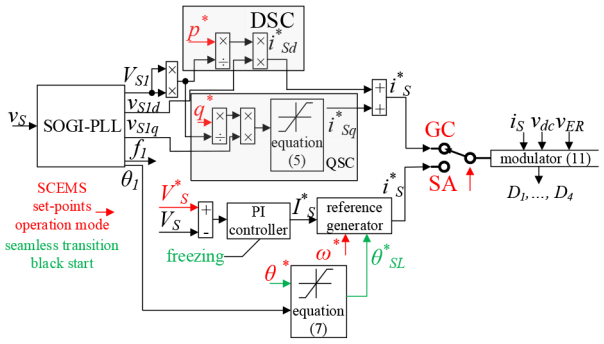

Fig. 6 *Block diagram of the DC–AC converter control strategy*

the main aim of maintaining the battery health. In this work, as a single ESS is involved in the ER, a control strategy similar to the one presented in [10, 11] was selected. The block diagram of the implemented strategy to generate the proper reference current (i^*_{ESS}) to be tracked by the bidirectional buck–boost DC–DC converter is depicted in Fig. 4. i^*_{ESS} is composed of adding two terms:

i. The main term ($i^*_{ESS\_1}$) is obtained as the current needed to meet the active power balance (neglecting the losses) on the ESS side and determined by the SCEMS ESS set-point

$$i^*_{ESS\_1} = \frac{p^*_{ESS}}{v_{ESS}}, \tag{1}$$

where p^*_{ESS} and v_{ESS} are the ESS reference power and the sensed ESS voltage, respectively.

ii. The second term ($i^*_{ESS\_2}$) regulates the DC-link voltage (v_{dc}) at the reference value (v^*_{dc}) as well as to compensate the power losses and the small deviations in the estimation of the plant parameters. This $i^*_{ESS\_2}$ is obtained from the output of a fast proportional–integral (PI) regulator.

Therefore, the active power balance and p^*_{ESS} is accomplished on the SC side, fitting on the ESS side as well. That is, the demanded/injected power from/to the ESS (p_{ESS}) will be higher or smaller than p^*_{ESS}, depending on the discharging or charging ESS operation, respectively.

With the goal to maintain the ESS state of health (SoH), reducing the ESS stress, a charging and discharging limitation must be considered. Besides, the system cannot surpass the maximum apparent power in any power converter ($s_{MAX,i}$). In this sense, the saturation block in Fig. 4 is justified as follows:

i. The ESS must be operated within healthy SoC limits, which depends on the ESS technology, but, roughly, it can be assumed limits between the 20 and 80% of the ESS rated capacity (Q_{ESS}).

ii. Once p^*, q^* (in GC mode), V^*, ω^* (in SA mode) and p^*_{pv} are set, the SCEMS selects a priority condition for the ER. The priority condition is based on the fact that $s_{MAX,i}$ in any power converter cannot be exceeded. The active and reactive power priorities are considered. If the reactive power priority is activated (just considered in GC mode), p^*_{ESS} must saturate its value to avoid ER overcurrent in the inverter as

$$p^*_{ESS} \leq \sqrt{s^2_{MAX,\,inv} - p^2_{pv} - q^2}, \tag{2}$$

where $s_{MAX,inv}$ is the $s_{MAX,i}$ of the inverter, p_{pv} is the extracted power from the PV and q is the injected reactive power into the SC by the ER. The active power priority will be discussed further as it does not affect to the p^*_{ESS} saturation.

At the same time, decreasing charging/discharging i^*_{ESS} rates contributes to the SoH maintenance and to help to the DC-link stability. Ramp rate control of the v^*_{dc} is also considered for the DC link during the pre-charge process.

3.3 DC–AC control strategy

The ER can work as grid feeding in GC mode and as grid forming in SA mode. An overview of different control strategies for the DC–AC converter both in GC and SA operation is reported in [3]. The grid-feeding ER is designed to inject/demand power into/from the SC. The scheme of the grid-feeding ER is shown in Fig. 5*a*. In this case, the SCEMS sets p^* and q^* to be traded, synchronised with the voltage at the SC-PCC. The grid-forming ER is represented in Fig. 5*b*, where SCEMS sets V^* and ω^*. This general assumption and simplified ER and SC representation is intended to make the ER operate in any topology of SC, that is, in any configuration of DERs, ESSs and loads. An adequate performance of the whole SC would first depend on the SCEMS. The full local control strategy of the ER DC–AC converter is depicted in Fig. 6 and explained in the following sections.

3.3.1 GC control: Once p^* and q^* are set by the SCEMS, the ER accomplishes its p^* by a direct sinusoidal current control (SCC) strategy [10]. The expression for the direct (*d*) component of the ER reference current (i^*_{Sd}) is as follows:

$$i^*_{Sd} = \frac{p^*}{V^2_{S1}} v_{S1d}, \tag{3}$$

where v_{S1d} is the instantaneous value of the fundamental component of SC grid voltage and V_{S1} is its RMS value.

A second-order generalised integrator phase-locked loop is implemented to extract the fundamental component of the grid voltages.

The ER is also able to provide voltage support at the SC-PCC or the improvement of the SC global power factor. The SCEMS calculates q^* for each ER. A quadrature sinusoidal current control strategy [10], similar to the SCC is used for this purpose. In this case, the q component of the ER reference current (i^*_{Sq}) is derived as

$$i^*_{Sq} = \frac{q^*}{V^2_{S1}} v_{S1q}, \tag{4}$$

where v_{S1q} is the instantaneous value of the fundamental component of SC grid voltage, being +90° phase shifted from v_{S1d}.

Here, q^* must be saturated if the SCEMS establishes the active power as priority. To avoid surpassing $s_{MAX,inv}$, the following restriction is implemented:

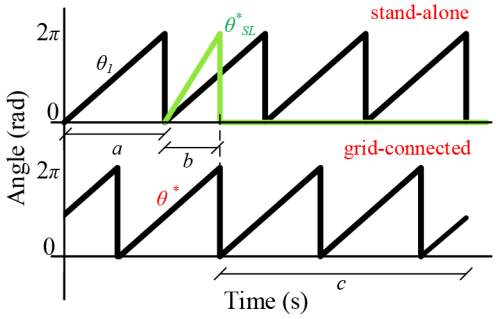

Fig. 7 *Synchronisation strategy for a seamless transition from SA to GC mode*

$$q^* \leq \sqrt{S^2_{\text{MAX, inv}} - (p_{\text{pv}} + p_{\text{ESS}})^2}\,. \tag{5}$$

3.3.2 SA control: If the SCEMS determines the SA mode operation, it sets V^* and ω^* to the low-level ER controllers.

A PI regulator assures the tracking of the RMS voltage reference, by acting over the peak value of the injected or demanded ER current (I^*_{S}). In this way, the same current controller than in GC mode can be used. The instantaneous reference current (i^*_{S}) in SA mode is calculated as

$$i^*_{\text{s}} = I_{\text{S}} \operatorname{sen}(\omega^* t)\,. \tag{6}$$

3.3.3 SA to GC transition: If the SC is operating in SA from the utility grid, but the SCEMS sends the references to the different dispersed ER as set-points in GC scenario, a pre-synchronisation and smooth transition between one mode and the other is required. If this pre-synchronisation is not carried out safely, inrush currents during the main switch turning-on action will make the protection system trip. A similar situation is presented during a black start, once a general blackout has taken place. In this case, the potential of distributed generation resources is used to help the power system restoration.

If a transition between GC and SA is required, the SCEMS sends the SC voltage grid phase (θ^*). The communication link between the SCEMS and ER low-level controller has a delay (t_{d}) that must be calculated. The ER voltage phase (θ_{l}) is locally obtained by a zero-crossing detection algorithm. With this, the voltage phase error (θ^*_{SL}) to be corrected during the resynchronisation time is defined as

$$\theta^*_{\text{SL}} = \theta^* + \omega t_{\text{d}} - \theta_{\text{l}}\,. \tag{7}$$

where ω is the pulsation of the utility grid. The duration of the resynchronisation can be selected as a function of the fundamental period (T_{f}). Depending on the SC goals and other conditions (e.g. type of load connected), this process can be shorter or longer. Thus, the incremental reference pulsation is calculated as

$$\Delta\omega^*_{\text{SL}} = \frac{\theta^* + \omega t_{\text{d}} - \theta_{\text{l}}}{n_{\text{p}} T_{\text{f}}}, \tag{8}$$

where n_{p} is the number of fundamental periods to produce the synchronisation.

The instantaneous reference current during the resynchronisation process with a seamless transition from SA to GC is determined as follows:

$$\begin{cases} i^*_{\text{S}} = I_{\text{S}} \operatorname{sen}(\omega t + \Delta\omega^*_{\text{SL}}) & \text{if } n < n_{\text{p}} \\ i^*_{\text{S}} = I_{\text{S}} \operatorname{sen}(\omega t) & \text{if } n \geq n_{\text{p}} \end{cases} \tag{9}$$

being n the current fundamental period. If $n = n_{\text{p}}$, the phase error between the grid voltage and ER voltage (v_{s}) is checked to be under the tolerance. This voltage phase correction during the resynchronisation process is graphically explained in Fig. 7, where a represents the duration of T_{f} and b the duration of resynchronisation.

At the same time, the PI regulator that adjusts I^*_{S} is frozen before the DSO switch turning-on. This mechanism helps the main grid to energise the power system. The time from the frozen reference at SA mode to the new reference in GC given by the SCEMS is also implemented with a ramp function. Operating in this way, a seamless transition between modes is achieved.

The ER duty cycles generation for both the ESS bidirectional buck–boost DC–DC and the DC–AC power converter, for tracking its set-points, is achieved by a deadbeat current controller.

Assuming that $v_{\text{s}}$is constant during the switching period (T_{c}) and solving the circuits presented in Fig. 2, the resulting expressions for calculating the ESS converter and the DC–AC converter duty cycles (D_{ESS} and D_{inv}) are, respectively

$$D_{\text{ESS}} = \left(v_{\text{ESS}} - i_{\text{ESS}} R_{\text{LESS}} - L_{\text{ESS}} \frac{i^*_{\text{ESS}} - i_{\text{ESS}}}{T_{\text{C}}}\right) \frac{1}{v_{\text{dc}}} \tag{10}$$

$$D_{\text{inv}} = \left(i_{\text{S}} R_{\text{L}} + Li \frac{i^*_i - i_i}{T_{\text{C}}} + \frac{v_{\text{s}}}{2} + 2v_{\text{dc}}\right) \frac{1}{2v_{\text{dc}}}\,. \tag{11}$$

4 Simulation analysis

This section verifies the described topology and the proposed control strategy, as well as the main functionalities by simulations using PSCAD/EMTDC software. The ER is simulated by the electrical models and the main parameters are summarised in Table 1.

It is important to note that the required measurements are sampled to match with the control frequency rate implemented in the ER controllers, making the simulation more realistic for further real implementation. The simulation parameters are the same as that the ones used for the real ER deployment. The different scenarios considered and simulated are:

i. ER is in GC mode, PV system is working at MPP, ESS discharges and charges and the DC–AC converter injects active and reactive powers into the SC.
ii. ER is in GC mode, PV system is working at RPP, ESS discharges and charges and the DC–AC converter injects active and reactive powers into the SC.
iii. PV system is not available (e.g. during the night), ESS discharges and the DC–AC converter injects active and reactive powers into the SC.
iv. ER is in SA mode, PV system is working at MPP with loads of 500 and 1500 W. Depending on the load power, the ESS charges or discharges.
v. ER is in SA mode, PV system is working at RPP with loads of 500 and 1500 W. Depending on the load power, the ESS charges or discharges.
vi. Three ERs are connected to the same SC-PCC in GC mode. PV systems and ESSs are working according to the individual active and reactive power set-points [(p^*_1, p^*_2 and p^*_3) and (q^*_1, q^*_2 and q^*_3), respectively] given by the SCEMS.
vii ER seamless transition from SA to GC.

.

Table 1 Simulation and ER parameters

Parameter	Unit	Value	
v_{MPP} (array composed of two strings with four serial panels)	V	70	
P_{MPP}	W	1040	
v_{ESS} (eight lead–acid type in serial)	V	96	
Q_{ESS}	Ah	17	
R_{Lpv}	Ω	0.1	
L_{pv}	mH	5	
R_{LESS}	Ω	0.25	
L_{ESS}	mH	5	
R_L	Ω	0.2	
L	mH	10	
C_f	μF	3	
C_1	μF	4400	
v^*_{dc}	V	220	
V_{S1} (1:2 transformer)	V	115	
grid frequency (f_s)	Hz	50	
RPPT subroutine execution time (t_{pv})	*s*	0.2	
$\delta_{pv,0}$	pu	0.05	
k_{adp}	pu	2	
K_p and K_i (DC-link PI controller)	pu	0.01	1
K_p and K_i (voltage PI controller)	pu	0.02	0.5
T_c	kHz	15	
sampling rate	kHz	4	

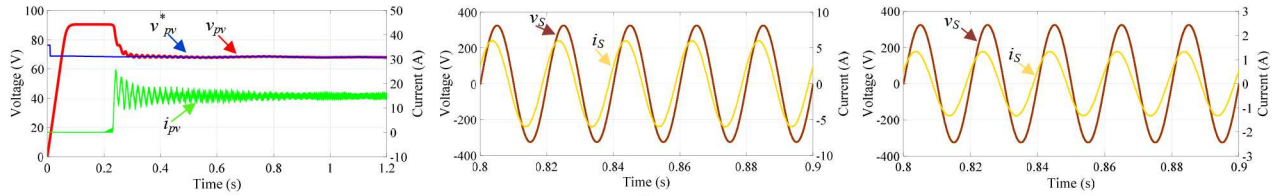

Fig. 8 *Scenario 1: simulated ER waveforms (MPP GC operation)*
(a) i_{pv}, v^*_{pv} and v_{pv}, ***(b)*** v_S and i_S, with set-points: $p^*_{ESS} = 500$ W, $p^* = 1330$ W and $q^* = 200$ VAr, ***(c)*** v_S and i_S, with $p^*_{ESS} = -500$ W, $p^* = 830$ W and $q^* = 200$ VAr

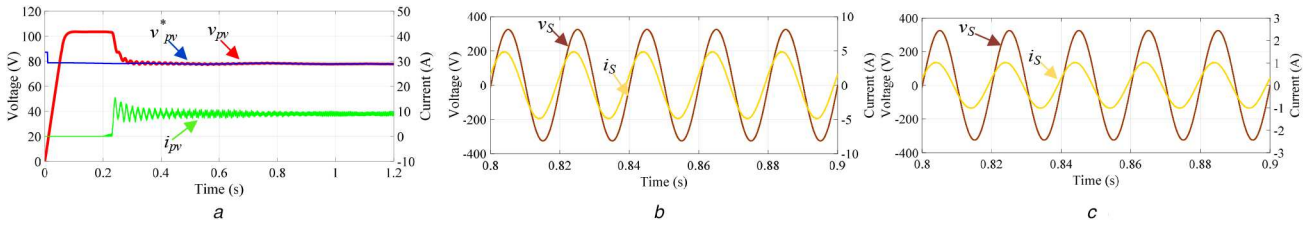

Fig. 9 *Scenario 2: simulated ER waveforms (680 W RPP GC operation)*
(a) i_{pv}, v^*_{pv} and v_{pv}, ***(b)*** v_S and i_S, with set-points: $p^*_{ESS} = 500$ W, $p^* = 1180$ W and $q^* = 200$ VAr, ***(c)*** v_S and i_S, with $p^*_{ESS} = -500$ W, $p^* = 180$ W and $q^* = 40$ VAr

The main ER waveforms obtained in the simulated scenarios 1 and 2 (both in GC mode) are presented in Figs. 8 and 9, respectively. The following set-points were obtained from the SCEMS, p^*_{pv} = MPP power, $p^*_{ESS} = 500$ and -500 W, $p^* = 1330$ and 830 W and $q^* = 200$ VAr for the first case. $p^*_{pv} = 680$ W, $p^*_{ESS} = 500$ and -500 W, $p^* = 1180$ and 180 W and $q^* = 200$ and 40 VAr for the second one. It is possible to observe that the steady-state waveforms (v_{PV} and i_S) tracks the reference values property.

Scenario 3 comprises the situation where the PV system is not available during the GC mode (Fig. 10). As there is not PV production, all the energy exchanged between the SC and ER is from the ESS. In Fig. 10*a*, the SoC_{ESS}, i^*_{ESS}, i_{ESS} and the ESS voltage are shown. Sinusoidal current is injected (Fig. 10*b*) or demanded (Fig. 10*c*).

The waveforms of the magnitudes of i_{pv}, i_{ESS}, v_S and i_S when the ER is operating in SA mode, with loads of 500 and 1500 W, are shown in Figs. 11 and 12. Two different scenarios are distinguished within the SA operation: the PV is working at MPP (scenario 4) and the PV is working at RPP (scenario 5). In both cases, the SCEMS sets $\omega^* = 50$ Hz and $V^*_S = 230$ V for the ER.

Fig. 13 depicts the delivered active and reactive powers to the SC-PCC [(p_1, p_2 and p_3) and (q_1, q_2 and q_3), respectively] by each of the three ERs under individual set-point steps. An accurate reference tracking and stable SC operation, with a small coupling between p and q are observed. Scenario 7 shows the pre-synchronisation process of the ER to provide a seamless transition from SA to GC (represented in Fig. 14). First, the SCEMS has set in SA the ω^* at 50 Hz and V^*_S = at 230 V_{rms}. At second 2, a new load is connected to the ER, being it capable to track the references accordingly. The adjustment of θ^*_{SL} to synchronise the SC and the utility grid starts at second 6.1. Seven fundamental periods were considered to eliminate the error between phase angles (this process ends around at 6.27 s). Finally, at second 6.3, the main

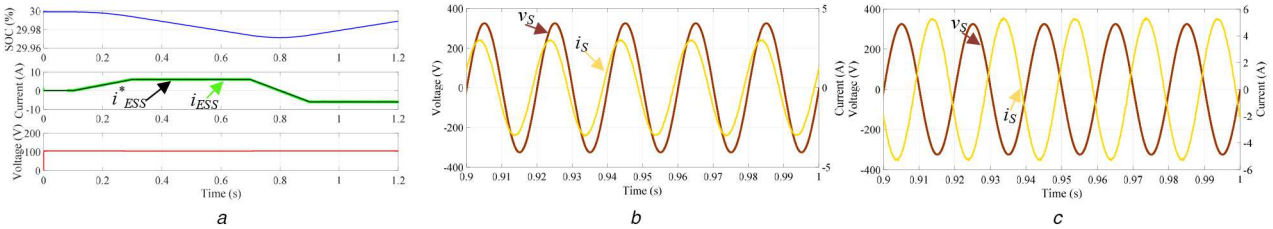

Fig. 10 *Scenario 3: simulated ER waveforms (PV unavailable GC operation)*
(a) From top to bottom: SoC_{ESS}, i_{ESS} and its reference i^*_{ESS} and v_{ESS}, ***(b)*** v_S and i_S, with set-points: $p^*_{ESS} = 600$ W, $p^* = 600$ W and $q^* = 100$ VAr, ***(c)*** v_S and i_S, with $p^*_{ESS} = -600$ W, $p^* = -600$ W and $q^* = 100$ VAr

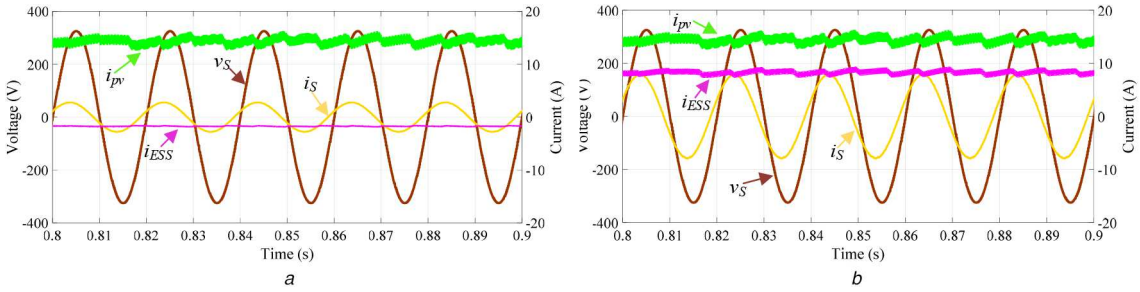

Fig. 11 *Scenario 4: Simulated ER waveforms (MPP SA operation)*
(a) i_{pv}, i_{ESS}, v_S and i_S, with load of 500 W, ***(b)*** i_{pv}, i_{ESS}, v_S and i_S, with load of 1500 W

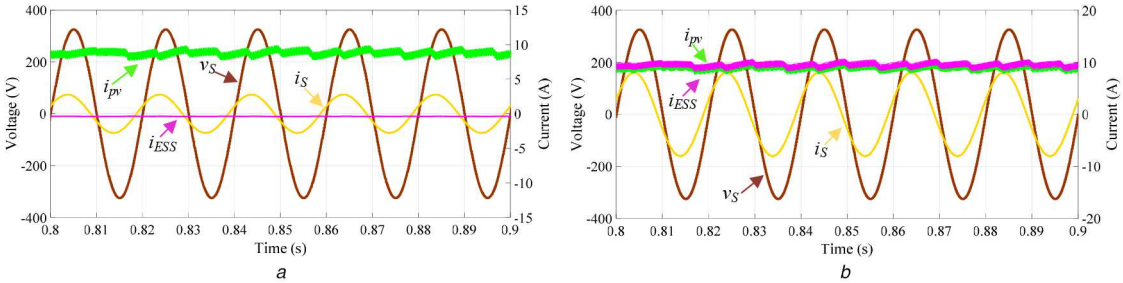

Fig. 12 *Scenario 5: Simulated ER waveforms (680 W RPP SA operation)*
(a) i_{pv}, i_{ESS}, v_S and i_S, with load of 500 W, ***(b)*** i_{pv}, i_{ESS}, v_S and i_S, with load of 1500 W

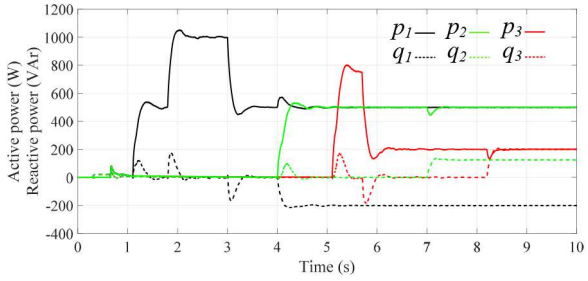

Fig. 13 *Scenario 6: p_1, p_2, p_3 and q_1, q_2, q_3 of three ERs connected to the same SC-PCC in GC mode*

switch is turned-on while I^*_S is frozen, maintaining the same value than in SA mode. Later, the new reference in GC given by the SCEMS is progressively achieved with a ramp function. No undesired transients are presented in this action. The simulation results confirm the theoretical predictions and the implemented flexible strategy in the considered scenarios.

5 Experimental results

This section encompasses the development and setup of the ER prototype. It has been experimentally tested in the same simulation scenarios, for a proper comparison and operating analysis.

An experimental prototype of the ER has been assembled, tested and finally deployed into an SC. The ER was installed inside a cabinet (Fig. 15). At the same time, the printed circuit boards and components were assembled with a high level of modularity, to facilitate the repairs. The insulated-gate bipolar transistors selected for the power electronic converters were the FUJI ELECTRIC 2MBI100TA-060-50 branch module, driven by the SKYPER 32 driver. The measurement board has been implemented by Hall-effect transducers, with galvanic isolation, LAH 25-NP for measuring DC and AC currents and LV 25-P for measuring DC and AC voltages, both from the manufacturer LEM. Those sensors work with high precision, good linearity and low common-mode disturbance.

The laboratory tests were made with a solar array emulator Chroma 62000H-S and an ESS composed of a serial connection of eight lead–acid-type batteries.

Similar scenarios than the presented in simulation were studied and tested. The first conducted tests aim to validate the ER operation in GC mode with p^*_{pv} = MPP power, $p^*_{ESS} = 500$ and -500 W, $p^* = 1330$ and 830 W and $q^* = 200$ VAr (scenario 1, in Fig. 16) and with $p^*_{pv} = 680$ W, $p^*_{ESS} = 500$ and -500 W, $p^* = 1180$ and 180 W and $q^* = 200$ and 40 VAr (scenario 2, in Fig. 17). The references given by the SCEMS were satisfied. Sinusoidal currents are injected into the SC with a total harmonic distortion

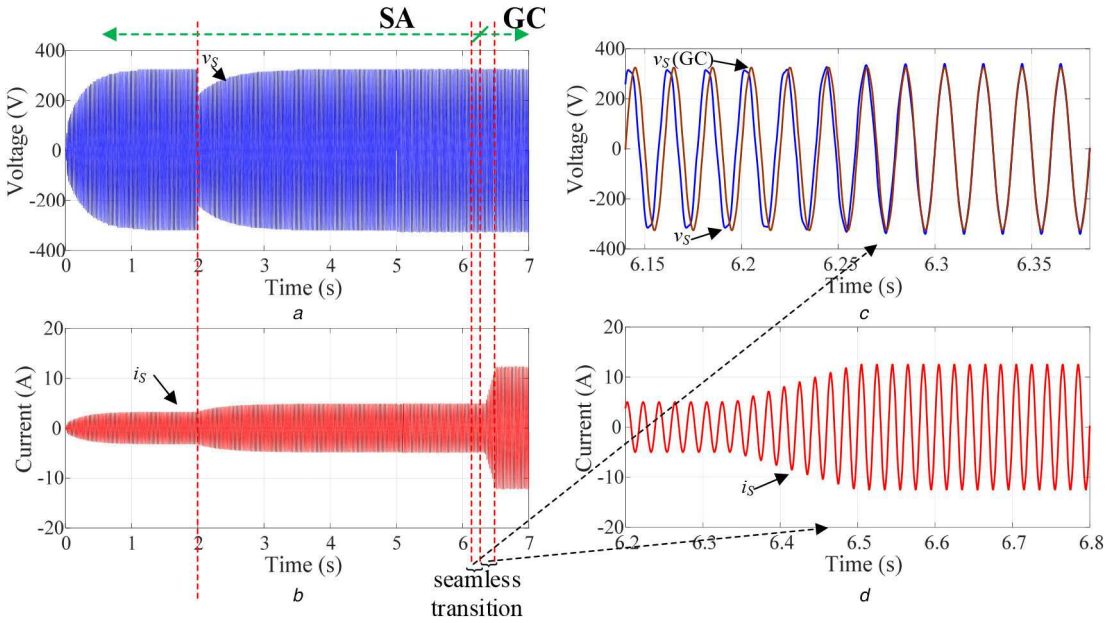

Fig. 14 *Scenario 7: Simulation of the ER waveforms during a black-start operation (transition from SA to GC)*
(a) v_S, ***(b)*** i_S, ***(c)*** ER voltage and resynchronisation process with v_S, ***(d)*** i_S during the resynchronisation process

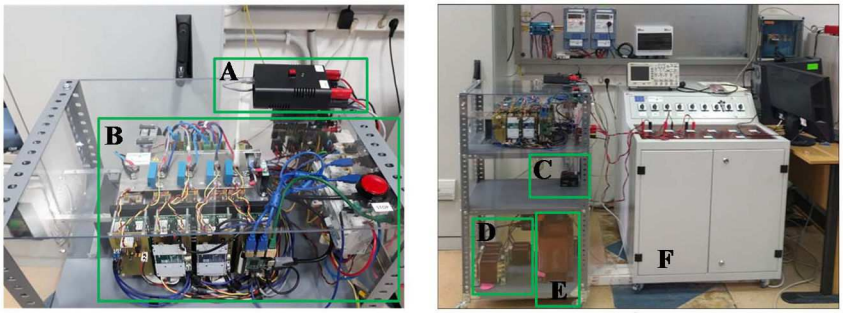

Fig. 15 *ER prototype*
(a) ER top view (A – $S_{SC–PCC}$, B – PV, ESS and grid power converters, and measurement and control boards), ***(b)*** ER cabinet full front view with ESS (C – auxiliary power supply, D – filters, E – transformer and F – ESS)

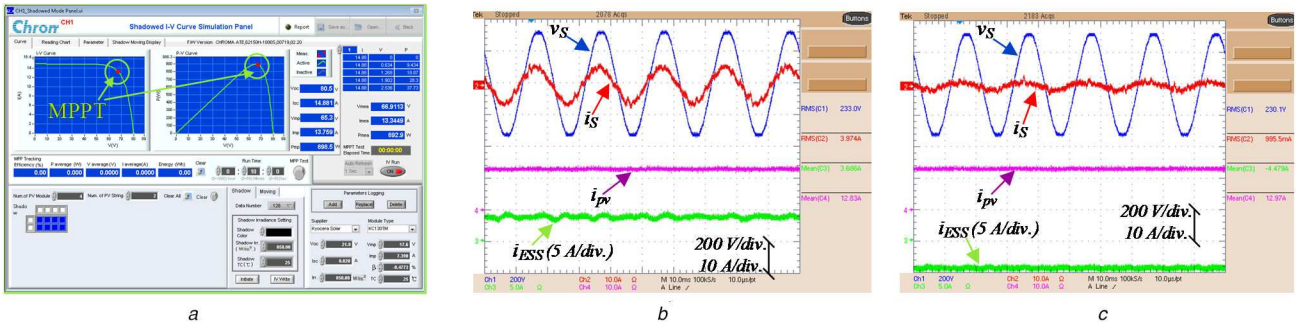

Fig. 16 *Scenario 1: Experimental ER waveforms (MPP GC operation)*
(a) Chroma emulator interface, ***(b)*** i_{ESS}, v_{pv}, v_S and i_S, with set-points: $p^*_{ESS} = 500$ W, $p^* = 1330$ W and $q^* = 200$ VAr, ***(c)*** i_{ESS}, v_{pv}, v_S and i_S with $p^*_{ESS} = -500$ W, $p^* = 830$ W and $q^* = 200$ VAr

below 5. At the same time, the current ripple obtained both in i_{pv} and i_{ESS} are within the design limits. Fig. 18 shows the main waveforms obtained if the PV is unavailable in GC mode (scenario 3), with set-points: (a) $p^*_{ESS} = 600$ W, $p^* = 600$ W and $q^* = 100$ VAr and (b) with $p^*_{ESS} = -600$ W, $p^* = -600$ W and $q^* = 100$ VAr.

The steady-state waveforms of i_{pv}, i_{ESS}, v_S and i_S during the SA mode, with connected loads of 500 and 1500 W, respectively, are shown in Fig. 19 (scenario 4) and Fig. 20 (scenario 5). References set at $\omega^* = 50$ Hz and $V^*_S = 230$ V_{rms} are successfully tracked.

Finally, the black start with pre-synchronisation process of the ER to provide a seamless transition from SA to GC was demonstrated in scenario 6. Fig. 21 shows the long-term experimental results (extracted from the SCEMS data) during a black start. Figs. 21*a–d* depict, respectively, the PV power, the ESS power the active power trading with the utility grid and the reactive power. In event 1, the PV system starts to work at MPP and all the power is stored in the ESS. Then, a 300 W load is connected to the ER, and ESS charging rate is reduced accordingly (event 2). After some time, the pre-synchronisation action is properly carried out and the DSO switch is switched on (3). Progressively, the PV power start to charge the ESS with the maximum power as the utility grid feed the SC. Event 4 is the control change from voltage

to current control (ER acts as grid-feeding unit). After event 5, the ER is disconnected.

Figs. 22 and 23 shows two different seamless transition processes. In the first case, the p^* for the GC mode is smaller than the load connected in SA. In this case, once the pre-synchronisation has finished, the current reference is frozen and progressively reduced. Similarly, but in opposite direction, the current reference is frozen and progressively increased in a case, where p^* is higher than in the GC mode is higher than the load connected in SA. Different time-scale views are shown in Figs. 22*a–c* and 23*a–c*. An effective smooth transition during the main switch turning-on process is demonstrated.

Finally, Fig. 24 shows some ER efficiency curves as a function of the power level. Firstly, the weighted California Energy Commission (CEC) efficiency of the PV system and the SC interface (see Fig. 1) was tested with the solar array emulator. The efficiency of these two power converters is measured at six power levels (i.e. 10, 20, 30, 50, 75 and 100% of the nominal power) and

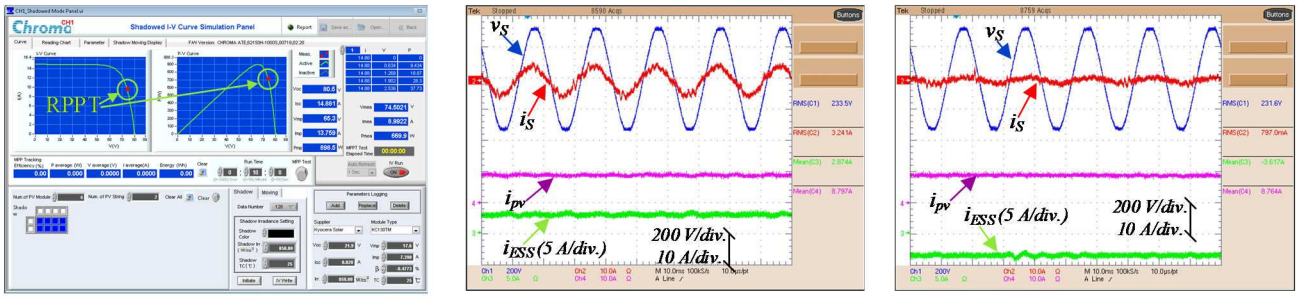

a b c

Fig. 17 *Scenario 2: Experimental ER waveforms (RPP 680 W GC operation)*
(a) Chroma emulator interface, ***(b)*** i_{ESS}, v_{pv}, v_S and i_S, with set-points: $p^*_{ESS} = 500$ W, $p^* = 1180$ W and $q^* = 200$ VAr, ***(c)*** i_{ESS}, v_{pv}, v_S and i_S with $p^*_{ESS} = -500$ W, $p^* = 180$ W and $q^* = 40$ VAr

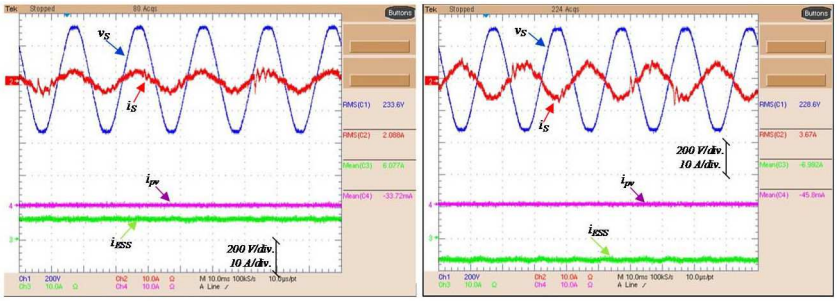

a b

Fig. 18 *Scenario 3: Experimental ER waveforms (PV unavailable GC operation)*
(a) i_{ESS}, v_{pv}, v_S and i_S, with set-points: $p^*_{ESS} = 600$ W, $p^* = 600$ W and $q^* = 100$ VAr, ***(b)*** i_{ESS}, v_{pv}, v_S and i_S, with $p^*_{ESS} = -600$ W, $p^* = -600$ W and $q^* = 100$ VAr

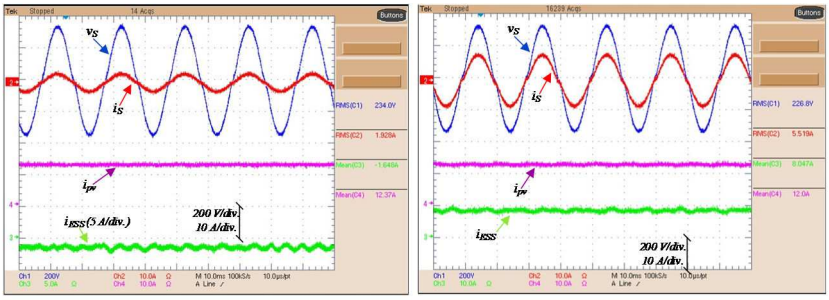

a b

Fig. 19 *Scenario 4: Experimental ER waveforms (MPP SA operation)*
(a) i_{pv}, i_{ESS}, v_S and i_S, with load of 500 W, ***(b)*** i_{pv}, i_{ESS}, v_S and i_S, with load of 1500 W

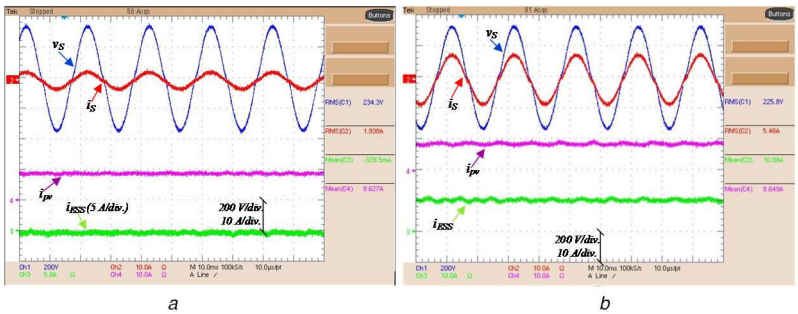

a b

Fig. 20 *Scenario 5: Experimental ER waveforms (RPP 680 W SA operation)*
(a) i_{pv}, i_{ESS}, v_S and i_S, with load of 500 W, ***(b)*** i_{pv}, i_{ESS}, v_S and i_S, with load of 1500 W

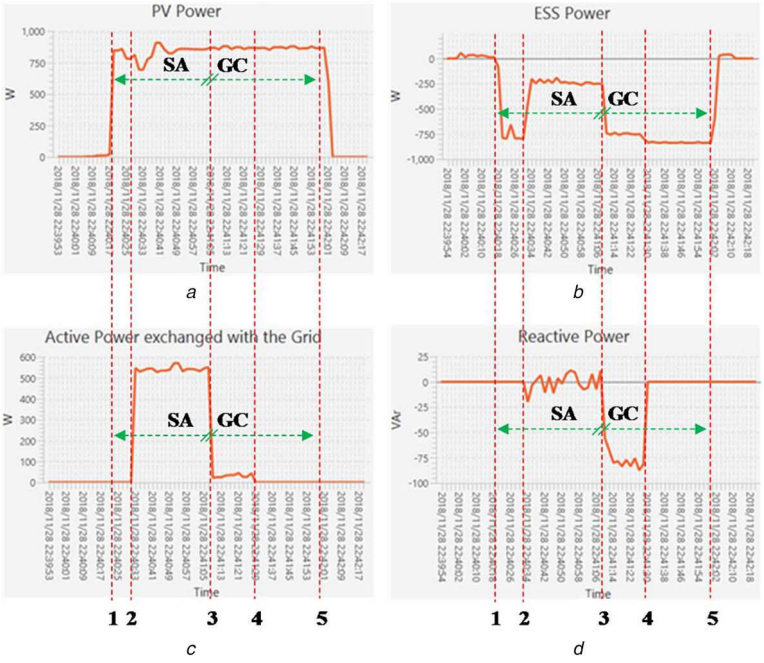

Fig. 21 *Scenario 7: Experimental results during a black-start operation (transition from SA to GC)*
(a) PV power, ***(b)***ESS power, ***(c)*** *p* trading with the SC, ***(d)*** *q* trading with the SC

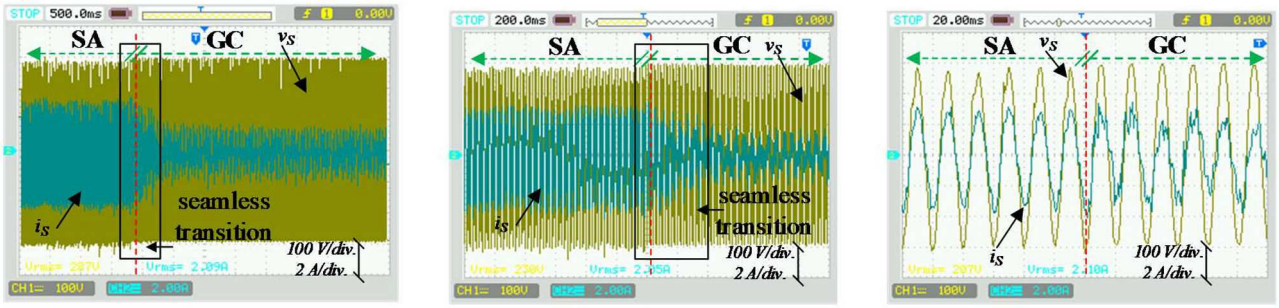

Fig. 22 *Scenario 7: Experimental v_S and i_S during a black-start operation with seamless transition when i^*_s is smaller in GC mode than in SA mode*
(a) Full view of the process, ***(b)*** Some fundamental period view, ***(c)*** Waveforms detail

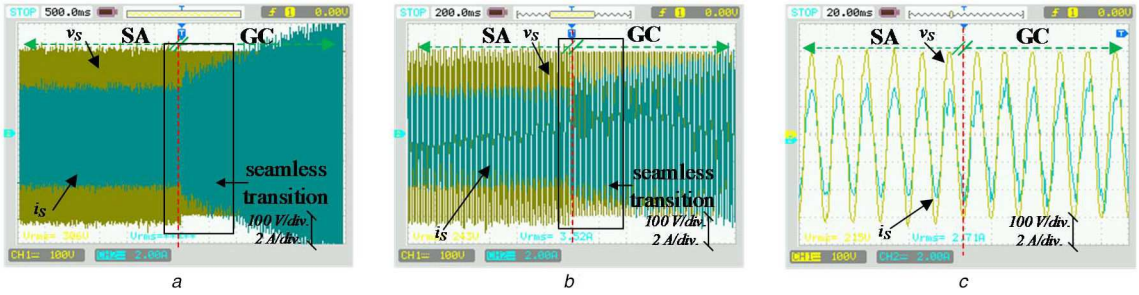

Fig. 23 *Scenario 7: Experimental v_S and i_S during a black-start operation with seamless transition when i^*_s is higher in GC mode than in SA mode*
(a) Full view of the process, ***(b)*** Some fundamental period view, ***(c)***Waveforms detail

at three values of v_{pv} [50 V (black line), 70 V (green line) and 90 V (yellow line)] for a total of 18 measurements. The CEC efficiency exceeds 92% under most operating conditions. Finally, the ER efficiency considering the PV and ESS systems were measured and computed (red line). This test was conducted by considering the PV system working at the MPP and ESS at the same six different power levels previously mentioned. The proposed ER achieves a maximum efficiency of 87.1%.

6 Conclusion

A flexible control strategy for a single-phase ER operating into an SC context has been proposed, implemented and validated. The strategy allows the ER to work in GC and in SA, providing a seamless transition from GC to SA, e.g. if a black start has taken place affecting the SC. The adjustment of the ER references is carefully analysed to make this process safe and accurate. At the same time, the ER is able to provide ancillary services to the SC as SC voltage support and global power factor improvement. The active power flow between the PVs and ESS, to increase the ER controllability, while maintaining the ESS SoH is considered, to increase the controllability of the ER, maintaining the ESS SoH. The simulation and experimental verification show the correct operation of the ER.

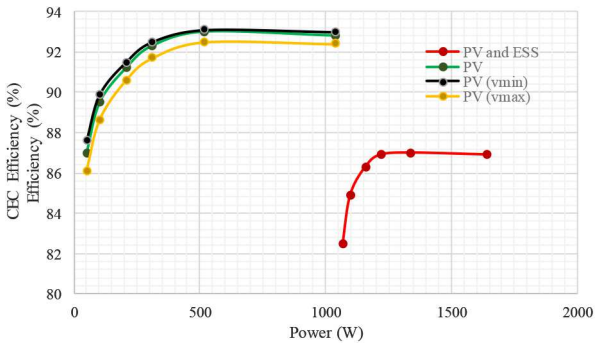

Fig. 24 *Measured efficiency of the ER prototype under different power levels and different input voltage*

7 Acknowledgments

The research work leading to these results has received funding from the Portuguese National Funds through FCT – Fundação para a Ciência e a Tecnologia in the context of the UID/EEA/00066/2019 project and from the European Union's Horizon 2020 research and innovation programme under Grant agreement no. 731155 – Storage4Grid project. The sole responsibility of this publication lies with the authors. The European Union is not responsible for any use that may be made of the information contained therein. The authors also acknowledge to the Junta de Extremadura (Regional Government) within the programme 'Ayudas Talento' (TA18003) the co-support for this work.

8 References

[1] SETIS, Smart electricity grids. Available at https://setis.ec.europa.eu/related-jrc-activities/jrc-setis-reports/smart-electricity-grids, accessed April 2019

[2] Micallef, A., Spiteri-Staines, M.C., Guerrero, J.M.: 'Single-phase microgrid with seamless transition capabilities between modes of operation', *IEEE Trans. Smart Grid*, 2015, **6**, (6), pp. 2736–2745

[3] Rocabert, J., Luna, A., Blaabjerg, F., *et al.*: 'Control of power converters in AC microgrids', *IEEE Trans. Power Electron.*, 2012, **27**, (11), pp. 4734–4749

[4] Hou, X., Sun, Y., Lu, J., *et al.*: 'Distributed hierarchical control of AC microgrid operating in grid-connected, islanded and their transition modes', *IEEE Access*, 2018, **6**, pp. 77388–77401

[5] Guerrero, J.M., Vasquez, J.C., Matas, J., *et al.*: 'Hierarchical control of droop-controlled AC and DC microgrids – a general approach toward standardization', *IEEE Trans. Ind. Electron.*, 2011, **58**, (1), pp. 158–172

[6] Fazeli, A., Sumner, M., Christopher, E., *et al.*: 'Power flow control for power and voltage management in future smart energy communities'. Third Renewable Power Generation Conf. (RPG 2014), Naples, Italy, September 2014, pp. 1–6

[7] Good, N., Mancarella, P.: 'Flexibility in multi-energy communities with electrical and thermal storage: a stochastic robust approach for multi-service demand response', *IEEE Trans. Smart Grids*, 2019, **10**, (1), pp. 503–513

[8] Liu, Y., Hu, S.: 'Renewable energy pricing driven scheduling in distributed smart community systems', *IEEE Trans. Parallel Distrib. Syst.*, 2017, **28**, (5), pp. 1445–1456

[9] Liu, N., Yu, X., Wang, C., *et al.*: 'Energy sharing management for microgrids with PV prosumers: a Stackelberg game approach', *IEEE Trans. Ind. Inf.*, 2017, **13**, (3), pp. 1088–1098

[10] Milanés-Montero, M.I., Barrero-González, F., Pando-Acedo, J., *et al.*: Active, reactive and harmonic control for distributed energy micro-storage systems in smart communities homes', *Energies*, 2017, **10**, (448), pp. 1–11

[11] Milanés-Montero, M.I., Barrero-González, F., Pando-Acedo, J., *et al.*: 'Smart community electric energy micro-storage systems with active functions', *IEEE Trans. Ind. Appl.*, 2018, **54**, (3), pp. 1975–1982

[12] Liu, N., Yu, X., Wang, C., *et al.*: 'Energy-sharing model with price-based demand response for microgrids of peer-to-peer prosumers', *IEEE Trans. Power Syst.*, 2017, **32**, (5), pp. 3569–3583

[13] Gungor, V.C., Sahin, D., Taskin, K., *et al.*: 'Smart grid technologies: communication technologies and standards', *IEEE Trans. Ind. Inf.*, 2011, **7**, (4), pp. 529–539

[14] Roasto, I., Husev, O., Najafzadeh, M., *et al.*: 'Voltage-source operation of the energy-router based on model predictive control', *Energies*, 2019, **12**, (10), pp. 1–15

[15] Liu, B., Wu, W., Zhou, C., *et al.*: 'An ac–dc hybrid multi-port energy router with coordinated control and energy management strategies', *IEEE Access*, 2019, **7**, pp. 109069–109082

[16] Ren, L., Zhang, C., Du, M.: 'Power router based on conventional three-phase bridge inverter and DC–DC converter', *CIRED-Open Access Proc. J.*, 2017, **1**, pp. 391–394

[17] Liu, B., Chen, J., Zhu, Y., *et al.*: 'Distributed control strategy of a microgrid community with an energy router', *IET Gener. Transm. Distrib.*, 2018, **12**, (17), pp. 4009–4015

[18] Li, X., Guo, L., Li, Y., *et al.*: 'Flexible interlinking and coordinated power control of multiple DC microgrids clusters', *IEEE Trans. Sustain. Energy*, 2018, **9**, (2), pp. 904–915

[19] Tu, C., Xiao, F., Lan, Z., *et al.*: 'Analysis and control of a novel modular based energy router for DC microgrid cluster', *IEEE J. Emerg. Sel. Top. Power Electron.*, 2019, **7**, (1), pp. 331–342

[20] Liu, Y., Fang, Y., Li, J., *et al.*: 'Interconnecting microgrids via the energy router with smart energy management', *Energies*, 2017, **10**, p. 1297

[21] Radwan, A.A.A., Mohamed, A.R.I.: 'Networked control and power management of AC/DC hybrid microgrids', *IEEE Syst. J.*, 2017, **11**, (7), pp. 1662–1673

[22] Zhou, J., Zhang, H., Sun, Q., *et al.*: 'Event-based distributed active power sharing control for interconnected AC and DC microgrids', *IEEE Trans. Smart Grid*, 2018, **9**, (6), pp. 6815–6828

[23] Li, X., Guo, L., Li, Y., *et al.*: 'A unified control for the DC–AC interlinking converters in hybrid AC/DC microgrids', *IEEE Trans. Smart Grid*, 2018, **9**, (6), pp. 6540–6553

[24] Nikolakakos, I., Zeineldin, H., Shawky El-Moursi, M., *et al.*: 'Stability evaluation of interconnected multi-inverter microgrids through critical clusters', *IEEE Trans. Power Syst.*, 2016, **31**, (4), pp. 3060–3072

[25] Pulcherio, M., Illindala, M.S., Choi, J.: 'Robust microgrid clustering in a distribution system with inverter-based DERs', *IEEE Trans. Ind. Appl.*, 2018, **54**, (5), pp. 5152–5162

[26] He, J., Wu, X., Wu, X.: 'Small-signal stability analysis and optimal parameters design of microgrid clusters', *IEEE Access*, 2019, **7**, pp. 36896–36909

[27] Zhao, Z., Yang, P., Wang, Y.: 'Dynamic characteristics analysis and stabilization of PV-based multiple microgrid clusters', *IEEE Trans. Smart Grid*, 2019, **10**, (1), pp. 805–818

[28] Han, Y., Zhang, K., Coelho, E. A.: 'MAS-based distributed coordinated control and optimization in microgrid and microgrid clusters: a comprehensive overview', *IEEE Trans. Power Electron.*, 2018, **33**, (8), pp. 6488–6508

[29] Karimi-Ghartemani, M.: 'Universal integrated synchronization and control for single-phase DC/AC converters', *IEEE Trans. Power Electron.*, 2015, **30**, (3), pp. 1544–1557

[30] Delgado-Gomes, V., Martins, J.F., Lima, C., *et al.*: 'Towards the use of unbundle smart meter for advanced inverters integration'. IEEE 26th Int. Symp. Industrial Electronics (ISIE), Edinburgh, Scotland, 2017, pp. 1721–1724

[31] Wang, J., Ji, B., Deng, X., *et al.*: 'Steady-state and dynamic input current low-frequency ripple evaluation and reduction in two-stage single-phase inverters with back current gain model', *IEEE Trans. Power Electron.*, 2014, **29**, (8), pp. 4247–4260

[32] Miñambres-Marcos, V., Guerrero-Martinez, M.A., Romero-Cadaval, E., *et al.*: 'Grid-connected photovoltaic power plants for helping node voltage regulation', *IET Renew. Power Gener.*, 2014, **9**, (3), pp. 236–244

[33] Yongheng, Y., Blaabjerg, F., Wang, H., *et al.*: 'Power control flexibilities for grid-connected multi-functional photovoltaic inverters', *IET Renew. Power Gener.*, 2016, **10**, (4), pp. 504–513

[34] Esram, T., Chapman, P.L.: 'Comparison of photovoltaic array maximum power point tracking techniques', *IEEE Trans. Energy Convers.*, 2007, **22**, (2), pp. 439–449

[35] Miñambres-Marcos, V., Guerrero-Martinez, M.A., Barrero-González, F., *et al.*: 'A grid-connected photovoltaic inverter with battery-supercapacitor hybrid energy storage', *Sensors*, 2017, **17**, (1856), pp. 1–18

[36] Guerrero-Martinez, M.A., Milanés-Montero, M.I., Barrero-González, F., *et al.*: 'A smart power electronic multiconverter for the residential sector', *Sensors*, 2017, **17**, (1217), p. 1